Timescale of open-reservoir evolution beneath the south Cleft segment, Juan de Fuca ridge

Carole Cordier, Martial Caroff, Eric Rannou

Revised version submitted to Mineralogy and Petrology the 21st of June 2011

Timescale of open-reservoir evolution beneath the south Cleft segment, Juan de Fuca ridge.

Cordier Carole, Caroff Martial, Rannou Eric

C. Cordier (✉) and M. Caroff

Université Européenne de Bretagne, Université de Brest; UMR n°6538 "Domaines Océaniques" et IUEM; 6 avenue Le Gorgeu, C.S. 93837,

29238 Brest Cedex 3, France.

E_mail: cordier@.unisi.it

C. Cordier

Present address: Museo Nazionale dell'Antartide, Universita di Siena, Via Laterina 8,

53100 Siena, Italy.

E. Rannou

Université Européenne de Bretagne, Université de Brest; UMR n°6205 "Laboratoire de Mathématiques"; 6 avenue Le Gorgeu, C.S. 93837,

29238 Brest Cedex 3, France.

Abstract Lavas erupted at the southern end of the intermediate Juan de Fuca ridge (Cleft segment) are mostly cogenetic and their chemical diversity results from melt evolution in an open magma system. In the present study, we apply a theoretical model allowing the time evolution of this periodically recharged and tapped magma chamber to be estimated. In our mathematical procedure, the melt quantity supplied to the reservoir varies through time following a sinusoidal function. The rare earth element concentrations in the refilling melt were calculated on the basis of the REE distribution in lavas. This theoretical composition is akin to that previously estimated for a Mg#70 MORB from mineralogical and chemical data. Then, we approached the temporal evolution of the reservoir using a set of suitable parameters deduced from the geometry of the crust and magma system beneath the Cleft segment. Particularly, we considered two end-members scenarios for the melt repartition through the magma reservoir beneath the Cleft segment: the "gabbro glacier" model (crystal nucleation and growth occur within one single melt lens and crystals subside vertically and laterally) and the "sheeted sill" model (crystallization takes place within a network of connected sills located at various depths in the crust). We estimated that the magma chamber is refilled every thousand years and that the melt resides approximately one hundred years within the reservoir.

Keywords: oceanic crust; mid-ocean ridge basalts; magmatic periodicity; open-system reservoir; replenishment melt; residence time

Introduction

To develop quantitative models for magmatic systems beneath fast- and intermediate-spreading ridges, constraints on the timescales of processes such as melting, differentiation,

and crystallization are required. Temporal information is still difficult to estimate from geological and geochemical data. For two decades, more and more studies were based on samples collected from holes drilled into the upper oceanic crust (Wilson et al. 2006), from across-ridge profiles (Davis et al. 2008), from crust exposures along slightly tectonized fracture zones or propagating rifts (Karson et al. 2002a; Karson et al. 2002b; Pollock et al. 2005; Cordier et al. 2007), and from ophiolite exposures (Pallister and Hopson 1981; Smewing 1981; Einaudi et al. 2003). These studies provided constraints on the relative chronology of the volcanics and then on the time-related chemical variations in lavas erupted from a single ridge segment. Further seismological data have shown that, beneath spreading ridges, the melt lens is a dynamic object. Its volume and depth are tied to the eruption and replenishment cycles of the magma reservoir (Hussenoeder et al. 1996; Hooft et al. 1997; Singh et al. 1998). The vertical movements of the melt lens were also documented by petrological evidences of reheating, hydrous partial melting and assimilation of the base of the sheeted dikes (Gillis and Coogan 2002; Koepke et al. 2008; France et al. 2010). On the whole, these results evidence cyclic variations of the thermal state of the axial magma chamber, related to fluctuations of the balance between magma recharge and hydrothermal cooling beneath spreading ridges.

We propose here to characterize the rare earth element (REE) concentrations in melts that evolved in a postulated periodically refilled reservoir and to estimate the REE composition of the replenishment melt, the average crystallization rate, the period of magma recharge and the average magma residence time, using the mathematical procedure developed by Rannou et al. (2006). We will consider the lavas erupted at the southern end of Juan de Fuca ridge axis: those collected at and near the axis (Smith et al. 1994; Stakes et al. 2006) and those collected along the northern wall of the Western Blanco Depression, which truncates the crust accreted at the Juan de Fuca axis since 1.4 Ma (Cordier et al. 2007). In addition to

chemical data, the model resolution requires the estimation of some geological parameters (Fig. 1) related to the architecture of the crust and to the geometry of the magma reservoir. A broad approach of these parameters has already been discussed by Rannou et al. (2006). Here, their estimation will be made to consider the specificities of the reservoir beneath fast- and intermediate-spreading ridges. Indeed, it is well-established that beneath these ridges, the axial magma chamber includes one or several thin lens(es) of partially crystallized melt located just below the sheeted dike complex and overlying a partially molten region (Detrick et al. 1987; Sinton and Detrick 1992; Boudier et al. 1996). However, the role of this (these) melt lens(es) in the storage and differentiation of mid-ocean ridge basalts (MORBs) and in the accretion of the lower crust is still debated. The current models are represented by two end-members. According to the "gabbro glacier" model (GG, Fig. 1b), crystal nucleation and growth occur within one single melt lens and crystals subside vertically and laterally to form the lower crust as oceanic crust spreads away from the ridge axis (Henstock et al. 1993; Phipps Morgan and Chen 1993; Quick and Denlinger 1993; Henstock 2002). Conversely, the "sheeted sill" model (SS, Fig. 1c) considers that crystallization takes place *in situ* within a network of connected sills located at various depths in the crust and that the seismically imaged melt lens is simply the shallowest of them (Boudier et al. 1996; Kelemen et al. 1997; Korenaga and Kelemen 1998; Garrido et al. 2001). The relative efficiency of these two scenarios depends on the cooling rate of the lower oceanic crust and thus on the interplay between heat supply through melt recharge and heat extraction through conduction and hydrothermal circulations. In turn, these models have diverging consequences on the repartition of the amount of crystallization with depth and on the expected degree of differentiation of the melt refilling the upper melt lens. For example, if heat removal by hydrothermal circulations is more efficient from the base of the dyke complex than from deeper in the lower crust, the majority of crystallization probably will occur in the upper melt

lens rather than *in situ* within the gabbroic section. In this case, primitive melts will be delivered to the upper lens. In our modeling, we thus evaluated the role of *in situ* crystallization and, through the quantity of melt in the magma chamber, the respective contribution of the upper melt lens and of the lower sills during magma differentiation.

Open magma system beneath the southern Cleft segment of the Juan de Fuca ridge

Recent evolution documented by the geochemistry of the Cleft lavas

The Juan de Fuca ridge separates the Pacific and Juan de Fuca plates (Fig. 2a, inset). Its southern 60 km-long Cleft segment (45°03'N to 44°27'N) spreads at an intermediate rate (56 mm/y, Wilson 1993) and is bounded by the Vance segment on the north and the Blanco fracture zone on the south (Fig. 2a). The segment axis is characterized by a dome rifted by a large transient graben (Normark et al. 1983). Along the southern part of the segment, the graben floor is notched by a central narrow depression, named cleft or axial summit collapse trough, which results from the collapse of volcanic structures, lava lakes or thick volcanic flows (Chadwick and Embley 1998; Stakes et al. 2006). The roof of discrete melt lenses has been seismically imaged at ~2 km of depth into the crust and over 10 km-long continuous intervals (Canales et al. 2005; Canales et al. 2006). In the southern part of the Cleft segment, the melt lens would be 100-m thick and 900-m wide and partially crystallized, comprising only ~ 30 vol. % of melt (Canales et al. 2006).

The Cleft lavas are normal MORBs resulting from the partial melting of a depleted and quite homogeneous mantle source with constant melting extents (Smith et al. 1994; Stakes et al. 2006). The lavas display a large range of compositions (3.5 < MgO wt. % < 8, Fig. 2b) that are thought to mostly result from the differentiation of primary tholeiitic melts in

open-system magma reservoirs (Fig. 2c). The correlation between lava ages, degrees of differentiation, and latitudes (Fig. 2b, Smith et al. 1994) is consistent with the coexistence of several discrete magma chambers along the Cleft segment, as observed in seismic profiles (Canales et al. 2005), and with the increase of the melt lens crystallinity from north to south inferred from geophysical studies (Canales et al. 2006). In the northern part, young and primitive basalts prevail (Fig. 2b) and would originate from a recently recharged magma reservoir. Southward, lavas are more evolved (Fig. 2b) and would derive from a progressively waned chamber, in response of the decrease of the magma supply (Smith et al. 1994). Thus, along the segment, the magma chambers are in different stage of evolution, which can be interpreted as reflecting the cyclic evolution through time of the axial magma reservoirs, as already proposed for the East Pacific Rise by Lagabrielle and Cormier (1999) and for the north-south propagating spreading center of the North Fiji Basin by Caroff and Fleutelot (2003).

The southernmost magma chamber that we study is interpreted to be in a waning state. Dacitic glass has been collected at the intersection between the southern Cleft segment and the Blanco fracture zone (Fig. 2). The dacitic melt could correspond to a differentiated product erupted from cooler and distal edges of the melt lens while the composition in the central part of the lens was buffered by replenishment (Stakes et al. 2006). However, Cotsonika et al. (2005) proposed that dacitic melts might result from contamination of basaltic resident melts by rhyolitic ones issued from the partial melting of the hydrated basaltic crust. More recently, Wanless et al. (2010) suggested that MOR dacites result from extensive fractional crystallization combined with partial melting and assimilation of amphibole-bearing altered crust.

Past evolution documented by the Western Blanco Depression lavas

At the southern tip of the Cleft segment, the northern wall of the Western Blanco Depression (Fig. 2a) provides a window through the slightly tectonized upper oceanic crust accreted for 1.4 Ma to the north of the ridge-transform intersection (Wilson et al. 1984; Embley and Wilson 1992; Juteau et al. 1995; Karson et al. 2002b; Fig. 3a). A thick volcanic unit, made of basaltic pillow-lavas, massive flows, and sparse feeder dikes (Juteau et al. 1995; Karson et al. 2002b), overlies an intensively hydrothermalized sheeted-dike complex (Manac'h et al. 1999). The northern scarp provides an opportunity to study the temporal variations of the lava composition by considering that the vertical succession of the lavas records increasing ages with depth (Tivey et al. 1998; Pollock et al. 2005; Cordier et al. 2007; Fig. 3a).

Cordier et al. (2007) have shown that the lavas outcropping along the Northern Scarp are mostly cogenetic. The conclusions of their petrological and geochemical study confirmed that beneath the southern tip of the Cleft segment: (i) the melt evolution occurs in a complex magma chamber, with differentiated, H_2O-rich compositions achieved in the cooler solidification zones; (ii) the differentiation mainly results from fractional crystallization, coupled with magma mixing between basaltic and intermediate melts; (iii) the mixing events reveal the periodic recharge of the reservoir by mafic melts (Mg#=70) and this regime has governed the magmatic system over the last ~1.4 Ma (Fig. 3b).

These results on the lavas erupted both at the present time (Smith et al. 1994; Stakes et al. 2006) and over the last 1.4 Ma (Cordier et al. 2007) show that the magma chamber beneath the southern end of the Cleft segment fulfills the conditions required to apply the model of Rannou et al. (2006): (i) the chemical variations in the collected lavas derive from reservoir differentiation and the chemical effects attributable either to the mantle source heterogeneity or to variations of the melting degree can be considered negligible (Smith et al. 1994), except perhaps for the dacite genesis (Wanless et al. 2010); (ii) the time evolution of the processes

occurring in the reservoir can be approached from the spatial distribution of the lava chemistry, along the length of the Cleft segment (Fig. 2b) or vertically (Fig. 3b) along the Northern Scarp (Smith et al. 1994; Pollock et al. 2005; Cordier et al. 2007); (iii) the magma chamber has evolved in open system, with periodic melt inputs (Cordier et al. 2007).

Geomathematical modeling of the temporal evolution of the magma chamber beneath the southern Cleft segment

Properties and resolution steps of the model

In the next sections, we will approach the variations of melt quantities and compositions during the evolution of a periodically replenished and tapped steady-state magma chamber through differential equations, by using the model developed by Rannou et al. (2006). Incompatible trace elements (here rare earth elements) are especially suitable for such a modeling. The behavior of compatible elements is too much dependent on both the nature and the proportion of the fractionating minerals. The originality of the model comes from the use of a sinusoidal function to reproduce the continuous and smoothed variations through time of the quantity of melt refilling the reservoir. The volume of resident melt varies in response to the intrusion and controls the crystallized and extruded volumes (Fig. 1a). Rannou et al. (2006) showed that for a steady-state reservoir, the REE concentrations in melts expelled from such a reservoir vary continuously through time following a sinusoidal curve. Concentrations in incompatible elements are minimal just after the recharge of the system by mafic melts, and they progressively increase due to the fractional crystallization occurring between two recharge events. This approach reconciles both concepts about the open-system magma chambers, usually treated separately: periodic inputs (O'Hara 1977; O'Hara and

Mathews 1981) and continuous inputs (De Paolo 1981; Reagan et al. 1987). Here, indeed, the input is continuous but occurs at different rates.

Rannou et al. (2006) demonstrated that this model is especially suitable for modeling the evolution of natural systems since it isolates the signals that are geologically significant. For example, in a reservoir that is periodically recharged by melt of near constant composition, the effects of natural disturbances in the replenishment cycles are strongly attenuated and do not perturb significantly the calculated variation through time of the lava composition (Rannou et al. 2006: their Fig. 3). Noises in the input function behave like a high-frequency signal, attenuated by the magmatic system. In the same way, an occasional and short variation of the incompatible trace element composition of the refilling melt, traducing for instance a sudden wall-rock contamination, does not significantly modify the modeled composition of the lavas that evolve in the system. For example, Rannou et al. (2006) have considered a magmatic system assimilating a quantity of rocks (leucosome with 12 ppm Ce) corresponding to 10 % of the incoming melt (MORB with 3 ppm Ce) during a fifth of the period. The difference in output Ce concentrations does not exceed 7% with respect to the assimilation-free model: the lava concentration peak increases from 17.2 to 18.3 ppm of Ce just after the event, then to a damped value of 17.8 ppm at the following cycle. These properties thus allow considering a smoothed, mathematically simple sinusoid to model the magma recharge.

Rannou et al. (2006) divided the resolution procedure in two steps (Fig. 4). The different parameters and their units are listed in Table 1. The first resolution step requires the estimation of:

- the incompatible trace element concentrations in the cogenetic lavas that bound the compositional range of the dataset, regarded as representative of the expelled liquids during the open-system evolution of the reservoir (C^{E}_{min} and C^{E}_{max} for the element E, Table 1);

- the distribution coefficients between the global solid that crystallized and the melt (D^E);

- the ratio between expulsion and crystallization rates (r_e).

We introduced an additional parameter with respect to the model of Rannou et al. (2006) to take into account the complexity of the differentiation in the composite magma chambers beneath the spreading ridges. Indeed, the interstitial residual melts of the crystal mush zones can be extracted and mix with the resident melt. The chemical evolution resulting from such a mechanism – if exists – certainly differs from the pure fractional crystallization process, as considered by Rannou et al. (2006). Thus, we considered the reinjection into the melt lens of a fraction *f* of interstitial liquid that has evolved within the partially solidified zones (Table 1). The equations are adapted from Langmuir (1989) by replacing the bulk distribution coefficient D^E by the parameter z^E (Table 1 and Eq. 2 of Fig. 4). As expressed, z^E models possible chemical exchanges between interstitial liquids and surrounding crystals (Langmuir 1989). Caroff (1995) named *imperfect fractional crystallization* this mechanism of solutal convection with mineralogical reactions, the principles of which being close to those of the *reactive crystallization* model of Collier and Kelemen (2010).

The different data are introduced into Eq. 1 of Fig. 4, in which all the parameters are considered constant through time. In a first step, for each REE, we run iteratively the Eq. 1 with different values of C_i^E and β^E (internal parameter, see Table 1 and Rannou et al. 2006) until the maximum and minimum concentrations that are modeled match those measured in lavas (Rannou et al. 2006). The replenishment pulsation (ω) is arbitrarily fixed for this first step as it has no effect on the calculated C^E values. This is equivalent to model the variations of C^E in function of a dimensionless time. The REE concentrations in the replenishment melt (C_i^E) and the β^E value for each REE are estimated. The average of the β^E values calculated for all the considered REE (β_{av}) corresponds to the ratio between the replenishment pulsation and

the crystallization rate (Table 1). The good reproducibility of the β^E values, i.e. a low standard deviation on their average $\sigma(\beta_{av})$, is then used to validate the set of distribution coefficients.

The second step of the modeling requires the estimation of the mean rate of melt injection [q_i] into the reservoir and of the variation of the quantity (here expressed as volume) of resident melt during a cycle (Q_{max}-Q_{min}). These parameters are introduced in Eqs. 3-5 (Fig. 4), together with r_e and β_{av}, to calculate the fraction of melt crystallized by year (α), the period of the replenishment (T), and the mean residence time of the melt within the reservoir (τ). By introducing these results in Eq. 6 (Fig. 4), we model the temporal variations of the resident melt volume.

The curves of Fig. 5 illustrate the effects of the variation of some parameters introduced into the modeling (C^E_{max}, f, Q_{max}-Q_{min}) on the calculated compositions of melt expelled from the periodically recharged reservoir (from Eq. 1: Fig. 5a, b) and on the volumes of resident melt (from Eq. 6: Fig. 5c, d).

Procedure applied to the magma system beneath the southern Cleft segment

Model parameter estimation

Our calculations are only based on rare earth elements (REE) because (i) these elements have been extensively analyzed in the available samples, (ii) their concentrations have not been significantly modified during subsequent seawater alteration, and (iii) their individual mineral/liquid distribution coefficients are quite well constrained from literature data. Along the Northern Scarp, Cordier et al. (2007) defined a cogenetic suite that extends from the mafic basalt BV2960-7 (MgO~8.1 wt.%) to the ferrobasalt BN02-12 (MgO~4.32 wt.%), both aphyric (Figs 2c and 6). We used these two samples to approach C^E_{min} and C^E_{max}, respectively

275 (Table 2). However, Cordier et al. (2007) found that some ferrobasalts might result from
276 mixing between dacitic residual melts (MgO~1.1 wt.%) and mafic melts (MgO~8.5 wt.%).
277 Even if such a hypothesis is judged unlikely in recent studies, such as Wanless et al. (2010), a
278 second set of calculations has been performed using a more evolved C^{E}_{max} end-member, in
279 view to test the response of the model to a variation of the chemical parameters introduced
280 into Eq. 1 of Fig. 4. All along the south Cleft segment, the only dacitic glass has been sampled
281 by Stakes et al. (2006) but has not been analyzed for REE by these authors (Table 2, Fig. 2,
282 sample RC10). Consequently, we used the composition of an andesite collected on the
283 Galapagos Spreading Center (Fornari et al. 1983; Perfit et al. 1983), that has REE pattern
284 parallel to the Northern Scarp ferrobasalts (Table 2 and Fig. 6a).
285 The next parameter, r_e (Table 1), has been approximated following the method
286 proposed by Rannou et al. (2006) as the ratio between the thicknesses of the basaltic and
287 gabbroic layers of the oceanic crust (Figs. 1b and c). Assuming that the gabbros extend from
288 the seismically imaged melt lens to the Moho, the ratio of the melt lens depth (2 km, Canales
289 et al. 2005) to the thickness of the plutonic complex (5 km, West et al. 2003) provides a r_e
290 ratio equal to 0.4.
291 The REE bulk distribution coefficients have been calculated by weighting the
292 individual mineral/liquid distribution coefficients of the mineral phases (Agee 1990; Fujimaki
293 et al. 1984) by their appropriate proportion in the global crystallizing assemblage. For a
294 differentiation leading to ferrobasalts, the phase proportions are determined for a Fe-Ti oxide-
295 free gabbroic cumulate (D_1^{E}, Table 2). For an andesitic term, the crystallizing assemblage
296 includes Fe-Ti oxides, as suggested by the drastic drop in the TiO_2 content observed in the
297 Fig. 3 diagram, and apatite (D_2^{E}, Table 2).
298 By varying the *f* value from 0 to 1, we can describe all the cases ranging from perfect
299 equilibrium (restricted to the solidification zone) to perfect fractional crystallization. The

300 procedure described by Rannou et al. (2006) presupposes a f value equal to 1 ($z^E=D^E$). In our
301 calculations, we also tested the model with a value of f of 0.5.
302 The last parameters to be estimated are the melt quantities, here expressed as volumes.
303 Beneath the Cleft segment, the distribution of the axial crustal reflector imaging the melt lens
304 shows that the magma chamber is continuous over 5 to 10 km-long intervals, even if its
305 characteristics (depth and crystallinity) vary with shorter wavelength (Canales et al. 2005). It
306 is likely that the scale of the magma chamber segmentation has not changed significantly over
307 the last thousands of years. Thus, we calculated the different melt volumes introduced in the
308 model resolution by considering a 10-km long magma chamber.
309 The mean rate of melt injection [q_i] is regarded as the volume of crust accreted per
310 year. For a 7 km-thick crust (West et al. 2003) and a full spreading rate of 56 mm/yr (Wilson
311 1993), [q_i] is equal to 0.004 km^3/(yr.10km).
312 The variation of the volume of resident melt during a cycle (Q_{max}-Q_{min}) is the least
313 precisely estimated, because it requires assumptions on the quantity of melt expellable from
314 the magmatic system and thus on the melt distribution over the crust thickness beneath the
315 ridge axis. Beneath the southern part of the Cleft segment, given the lens size and crystallinity
316 deduced from seismic data (Canales et al. 2005, 2006), the quantity of melt that can be
317 expelled from the uppermost, seismically imaged and partially crystallized lens (gabbro
318 glacier model GG1, Fig. 1b) during the time interval of inflation and deflation of the magma
319 chamber is ca. 0.45 km^3 (Table 3). We also run the calculations with a higher volume of melt
320 (0.63 km^3/10 km, GG2, Fig. 1b and Table 3) to consider the partial draining of the interstitial
321 melt from the mushy solidification zones to the melt lens during compaction of the magma
322 chamber (Lagabrielle and Cormier 1999). Finally, we made an attempt to estimate the volume
323 of melt expellable from several sheeted sills distributed all over the crust thickness (SS model,
324 Fig. 1c). However, no geophysical results can be actually used to decide how many sills lie in

depth and how these sills contribute to the magma chamber tapping. We arbitrarily considered that no more than a second melt lens is affected by the melt tapping, assigning a value of 0.9 km^3/10 km to the parameter Q_{max}-Q_{min} (Table 3).

Results

The geochemical and temporal results of the modeling applied to the magma system beneath the southern Cleft segment are shown in Table 3 and in Figs 5-6. The consistency of the set of D^E (and z^E) coefficients, and consequently the validity of the calculated C_i^E, is attested by the good reproducibility of the β^E values calculated for the different REE (Table 3), as shown by the low $\sigma(\beta_{av})$ values (ranging from 0.119 to 0.200, Table 3). For a *f* value of 1, the C_i^E values calculated from the ferrobasalt and andesite composition to approach C^E_{max} are fairly similar (Table 3 and Fig. 6b). The C_i^E patterns have lower REE contents and are slightly more depleted in light REE relative to lavas. The pattern of the primary melt with Mg#=70 determined by Cordier et al. (2007) is very close to and bracketed by the two theoretical refilling melt compositions (Fig. 6b). This similarity confirms that the modeled replenishment liquid can be regarded as a primary melt.

The differentiation sequence leading to andesites cannot be reproduced using a low *f* value to model a low melt flow from the solidification zones to the main magma lens (Langmuir 1989, Caroff 1995). Indeed, for most of the REE (except La and Nd), the modeled composition of expelled melts does not match the observed composition range. This result might support that andesite/dacite compositions cannot be achieved by pure MORB fractional crystallization, consistently with the Wanless et al. (2010) conclusions. For the differentiation leading to ferrobasalts, introducing a *f* value of 0.5 results in C_i^E values slightly higher than

for perfect fractional crystallization (f=1, Fig. 5b), without significant increase of the β^E variability ($\sigma(\beta_{av})$=0.124, Table 3).

When calculating the temporal data, the only varying parameters are β_{av} and Q_{max}-Q_{min} (Eqs 3-5, Fig. 4). Low β_{av}, resulting either from high C^E_{max} or from low f values (Table 1, Step 1), produces high average crystallization rate α, high replenishment period T, and low average melt residence time τ (Fig. 5a, b and Table 3, Step 2). Conversely, an increase of the variation of the magma chamber volume during a cycle (Q_{max}-Q_{min}) results in a diminution of α and an increase of both T and τ (Fig. 5c, d and Table 3, Step 2). Thus, considering a reservoir with a well-established thermal regime, the more the volume of interconnected (i.e. expellable) liquids is high the more the time required for magma differentiation is long. As the temporal results are very sensitive to the Q_{max}-Q_{min} value (Fig. 5 and Table 3), they strongly depend on the assumptions about the quantity of expellable melt.

The volume of melt in the reservoir oscillates through time with inflation plus deflation cycles of 550 to 2250 years, in function of the values ascribed to the chemical and geological parameters (Table 3 and Fig. 5). In average, melts reside 60 to 150 years in the magma chamber (Table 3). The variation range of the calculated magma residence times is close to that determined using Ra-Th disequilibria (tens to thousands years) for basaltic to andesitic magmas that have evolved in steady-state, well mixed, open-reservoirs (Pyle 1992). However, the temporal results of this modeling can hardly be validated by direct comparison with radiochronological data measured on the studied samples. First, we cannot estimate the cycle period by dating the mafic samples that bracket a chemical cycle. Current datation methods have not a sufficient time resolution (e.g. magnetic isochrones, Fig. 3), they are difficult to apply to tholeiites (e.g. K/Ar and $^{40}Ar/^{39}Ar$ methods), or they are not suitable for the considered lavas that are older than about 300 Ka (e.g. $^{230}Th/^{238}U$, Fig. 2). Second, our samples are too old (> 8,000 years) to still record the ^{226}Ra-^{230}Th or ^{210}Pb–^{226}Ra disequilibria,

374 which are generally used to estimate the magma residence time in spreading ridge context
375 (Cooper et al. 2003; Goldstein et al. 1993; Rubin and MacDougall 1990; Rubin et al. 2005;
376 Volpe and Goldstein 1993).
377
378 **Conclusions**
379
380 In this study, we attempted to model the time evolution of the periodically recharged magma
381 chamber beneath the southern tip of the Cleft spreading segment. First, Rannou et al. (2006)
382 developed a realistic mathematical procedure to model the geochemical evolution of changing
383 volume magma chambers, periodically recharged and tapped. Subsequently, in their study on
384 the lavas exposed along the northern wall of the Western Blanco Depression, Cordier et al.
385 (2007) highlighted a complex chemical evolution with depth, interpreted as the result of
386 periodic replenishment of the southernmost magma reservoir of the Cleft segment.
387 We applied here the procedure of Rannou et al. (2006) to this zone of the Cleft
388 segment. The composition of the replenishment melt that we modeled is consistent with that
389 obtained from mineralogical and chemical data for a Mg#=70 melt (Cordier et al. 2007). This
390 reproducibility between theoretical and experimental compositions, already shown by Rannou
391 et al. (2006) in their application to North Fiji Basin lavas, validates the first step of the
392 modeling. In addition, by introducing geological parameters in the modeling procedure, we
393 estimated that the magma chamber is refilled every 1,100 ± 500 years and that the melt
394 resides ~ 100 years within the reservoir beneath the southern Cleft segment. These temporal
395 results are close to those calculated in a same way for the ultra-fast spreading East Pacific
396 ridge (period T = 750 years and magma residence time τ = 300 years; Rannou et al. 2006).
397 This study demonstrates the applicability of the model of Rannou et al. (2006) to
398 magma reservoirs beneath spreading ridges. Once the periodic evolution of the magma

chamber demonstrated, it can be used to approach the composition of the replenishment melt. Besides, its application to sites where conventional dating methods are not relevant is an auxiliary approach to access the periodicity of the magmatic cycles and the melt residence time. The result accuracy depends on the precision when estimating the variable parameters, from geological and geochemical data. Inversely, for sites where our theoretical approach could be combined with radiochronological data, such a combination could bring new constraints on some of the data used for the model resolution and consequently on the subjacent assumptions about the magma system. For example, the volume of melt expellable from the magmatic system (Q_{max}-Q_{min}) could then be stated and the models of lower oceanic crust accretion be discriminated.

Acknowledgments: We acknowledge Johann G. Raith for editorial assistance and Wendy Bohrson for reviewing this work.

References

Agee CB (1990) A new look at differentiation of the Earth from melting experiments on the Allende meteorite. Nature, 346: 834-837

Boudier F, Nicolas A, Ildefonse B (1996) Magma chambers in the Oman ophiolite: Fed from the top or from the bottom? Earth and Planetary Science Letters 144: 239-250

Canales JP, Detrick RS, Carbotte SM, Kent GM, Diebold JB, Harding AJ, Babcock JM, Nedimovic MR, Van Ark E (2005) Upper crustal structure and axial topography at intermediate spreading ridges: Seismic constraints from the southern Juan de Fuca ridge. Journal of Geophysical Research, 110, B12104, doi: 10.1029/2005JB003630

Canales JP, Singh SC, Detrick RS, Carbotte SM, Harding AJ, Kent GM, Diebold JB, Babcock JM, Nedimovic MR (2006) Seismic evidence for variations in axial magma chamber properties along the southern Juan de Fuca Ridge. Earth and Planetary Science Letters 246: 353-366

Caroff M (1995) Open system crystallization and mixing in two-layers magma chambers. Lithos 36: 85-102

Caroff M, Fleutelot C (2003) The north-south propagating spreading center of the North Fiji Basin. Modeling of the geochemical evolution in periodically replenished and tapped magma chambers. Mineralogy and Petrology 79: 203-224

Chadwick W, Embley, RW (1998) Graben formation associated with recent dike intrusions and volcanic eruptions on the mid-ocean ridge. Journal of Geophysical Research 103: 9807-9825

Collier ML, Kelemen PB (2010) The case for reactive crystallization at Mid-Ocean Ridges. Journal of Petrology 51: 1913-1940

Cooper KM, Goldstein SJ, Sims KWW, Murrell MT (2003) Uranium-series chronology of Gorda ridge volcanism: new evidence from the 1996 eruption. Earth and Planetary Science Letters 206: 459-475

Cordier C, Caroff M, Juteau T, Fleutelot C, Hémond C, Drouin M, Cotten J, Bollinger C (2007) Bulk-rock geochemistry and plagioclase zoning in lavas exposed along the northern flank of the Western Blanco Depression (Northeast Pacific): Insight into open-system magma chamber processes. Lithos 99: 289-311

Cotsonika LA, Perfit MR, Smith MC, Kamenov GD, Stakes DS, Ridley WI, Wallace P (2005) The occurrence and origin of andesites and dacites from the Southern Juan de Fuca Ridge. Eos Transactions, American Geophysical Union, Fall Meeting Supplement 86 (18), Abstract V13A-04

448 Davis AS, Clague DAC., Cousens BL, Keaten B, Paduan JB (2008) Geochemistry of basalt
449 from the North Gorda segment of the Gorda Ridge: Evolution toward ultraslow
450 spreading ridge lavas due to decreasing magma supply. Geochemistry Geophysics
451 Geosystems 9, Q04004, doi: 10.1029/2007GC001775
452 De Paolo DJ (1981) Trace element and isotopic effects of combined wallrock assimilation and
453 fractional crystallization. Earth and Planetary Science Letters 53: 189-202
454 Detrick RS, Buhl P, Vera EE, Mutter JC, Orcutt JA, Madsen JA, Brocher TM (1987)
455 Multichannel seismic imaging of a crustal magma chamber along the East Pacific
456 Rise. Nature 326: 35-41
457 Einaudi F, Godard M, Pezard PA, Cochemé JJ, Coulon C, Brewer T, Harvey P (2003)
458 Magmatic cycles and formation of the upper oceanic crust at spreading centers:
459 Geochemical study of a continuous extrusive section in the Oman ophiolite.
460 Geochemistry Geophysics Geosystems 4, 8608, doi: 10.1029/2002GC000362
461 Embley RW, Wilson DS (1992) Morphology of the Blanco Transform Fault Zone-NE Pacific:
462 Implications for its tectonic evolution. Marine Geophysical Researches 14: 25-45.
463 Fornari DJ, Perfit MR, Malahoff A, Embley RW (1983) Geochemical studies of abyssal lavas
464 recovered by DSRV Alvin from eastern Galapagos rift, Inca transform and Ecuador
465 rift 1. Major element variations in natural glasses and spacial distribution of lavas.
466 Journal of Geophysical Research 88: 10519-10529
467 France L, Koepke J, Ildefonse B, Cichy SB, Deschamps F (2010) Hydrous partial melting in
468 the sheeted dike complex at fast spreading ridges: experimental and natural
469 observations. Contributions to Mineralogy and Petrology 160: 683-704
470 Fujimaki H, Tatsumoto M, Aoki KI (1984) Partition coefficients of Hf, Zr, and REE between
471 phenocrysts and groundmasses. Lunar and Planetary Science Conference, 14th,
472 Houston, TX, Journal of Geophysical Research, Supplement 89, B662-B672

473 Garrido C, Kelemen P, Hirth G (2001) Variation of cooling rate with depth in lower crust
474 formed at an oceanic spreading ridge: Plagioclase crystal size distributions in gabbros
475 from the Oman ophiolite. Geochemistry Geophysics Geosystems 2, 1041, doi:
476 10.1029/2000GC000136
477 Gillis KM, Coogan LA (2002) Anatectic migmatites from the roof of an ocean ridge magma
478 chamber. Journal of Petrology 43: 2075-2095
479 Goldstein SJ, Murrell MT, Williams RW (1993) ^{231}Pa and ^{230}Th chronology of mid-ocean
480 ridge basalts. Earth and Planetary Science Letters 115: 151-159
481 Henstock TJ (2002) Compaction control of melt distribution at fast-spreading mid-ocean
482 ridges. Geophysical Research Letters 29, 1137, doi: 10.1029/2001GL013755
483 Henstock TJ, Woods AW, White RS (1993) The accretion of oceanic crust by episodic sill
484 intrusion. Journal of Geophysical Research 98: 4143-4161
485 Hooft EEE, Detrick RS, Kent GM (1997) Seismic structure and indicators of magma budget
486 along the Southern East Pacific Rise. Journal of Geophysical Research 102: 27319-
487 27340
488 Hussenoeder SA, Collins JA, Kent GM, Detrick RS (1996) Seismic analysis of the axial
489 magma chamber reflector along the southern East Pacific Rise from conventional
490 reflection profiling. Journal of Geophysical Research 101: 22087-22105
491 Juteau T et al (1995) A submersible study in the Western Blanco Fracture Zone, N.E. Pacific:
492 structure and evolution during the last 1.6 Ma. Marine Geophysical Researches 17:
493 399-430
494 Karson JA et al (2002a) Structure of uppermost fast spread oceanic crust exposed at the Hess
495 Deep Rift: Implications for subaxial processes at the East Pacific Rise. Geochemistry
496 Geophysics Geosystems 3, 1002, doi: 10.1029/2001GC000155

497 Karson JA, Maurice AT, Delaney JR (2002b) Internal structure of uppermost oceanic crust
498 along the Western Blanco Transform Scarp: Implications for subaxial accretion and
499 deformation at the Juan de Fuca Ridge. Journal of Geophysical Research 107, 2181,
500 doi: 10.1029/2000JB000051
501 Kelemen PB, Koga KT, Shimizu N (1997) Geochemistry of gabbro sills in the crust/mantle
502 transition zone of the Oman ophiolite: Implications for the origin of the oceanic lower
503 crust. Earth and Planetary Science Letters 146: 475-488
504 Koepke J, Christie DM, Dziony W, Holtz F, Lattard D, Maclennan J, Park S, Scheibner B,
505 Yamasaki T, Yamasaki S (2008) Petrography of the dike-gabbro transition at IODP
506 Site 1256 (equatorial Pacific): The evolution of the granoblastic dikes. Geochemistry
507 Geophysics Geosystems 9: Q07O09, doi: 10.1029/2008GC001939
508 Korenaga J, Kelemen PB (1998) Melt migration through the oceanic lower crust: A constraint
509 from melt percolation modelling with finite solid diffusion. Earth and Planetary
510 Science Letters 156: 1-11
511 Lagabrielle Y, Cormier M-H (1999) Formation of large summit troughs along the East Pacific
512 Rise as collapse calderas: An evolutionary model. Journal of Geophysical Research
513 104: 12971-12988
514 Langmuir CH (1989) Geochemical consequence of in situ crystallization. Nature 340: 199-
515 205
516 Manac'h G, Lécuyer C, Juteau T (1999) A fluid inclusion and stable isotope study of
517 hydrothermal circulation in a transform zone: Western Blanco Depression, northeast
518 Pacific. Journal of Geophysical Research 104: 12941–12970
519 Normark WR, Morton JL, Koski R, Clague DA (1983) Active hydrothermal vents and sulfide
520 deposits on the southern Juan de Fuca Ridge. Geology 11: 158-163

O'Hara MJ (1977) Geochemical evolution during fractional crystallization of a periodically refilled magma chamber. Nature 266: 503-507

O'Hara MJ, Mathews RE (1981) Geochemical evolution in an advancing, periodically replenished, periodically tapped, continuously fractionated magma chamber. Journal of the Geological Society of London 138: 237-277

Pallister JS, Hopson CA (1981) Samail Ophiolite plutonic suite: Field relations, phase variation, cryptic variation and layering, and a model of a spreading ridge magma chamber. Journal of Geophysical Research 86: 2593-2644

Perfit MR, Fornari DJ, Malahoff A, Embley RW (1983) Geochemical studies of abyssal lavas recovered by DSRV ALVIN from Eastern Galapagos Rift, Inca Transform, and Ecuador Rift, 3, Trace element abundances and petrogenesis. Journal of Geophysical Research 88: 10551-10572

Phipps Morgan J, Chen YJ (1993) The genesis of oceanic crust: Magma injection, hydrothermal circulation, and crustal flow. Journal of Geophysical Research 98: 6283-6297

Pollock MA, Klein EM, Karson JA, Tivey MA (2005) Temporal and spacial variability in the composition of lavas exposed along the Western Blanco Transform Fault. Geochemistry Geophysics Geosystems 6, Q11009, doi: 10.1029/2005GC001026

Pyle DM (1992) The volume and residence time of magma beneath active volcanoes determined by decay-series disequilibria methods. Earth and Planetary Science Letters 112: 61-73

Quick JE, Denlinger RP (1993) Ductile deformation and the origin of layered gabbro in ophiolites. Journal of Geophysical Research 98: 14015-14027

544 Rannou E, Caroff M, Cordier C (2006) A geochemical approach to model periodically
545 replenished magma chambers: Does oscillatory supply account for the magmatic
546 evolution of EPR 17-19°S? Geochimica et Cosmochimica Acta 70: 4783-4796
547 Reagan MK, Gill JB, Malavassi E, Garcia MO (1987) Changes in magma composition at
548 Arenal volcano, Costa Rica, 1968-1985 : real-time monitoring of open-system
549 differentiation. Bulletin of Volcanology 49: 415-434
550 Rubin KH, MacDougall JD (1990) Dating of neovolcanic MORB using (^{226}Ra/^{230}Th)
551 disequilibrium. Earth and Planetary Science Letters 101: 313-322
552 Rubin KH, van Der Zander I, Smith MC, Bergmanis EC (2005) Minimum speed limit for
553 ocean ridge magmatism from ^{210}Pb–^{226}Ra–^{230}Th disequilibria. Nature 437: 534-538
554 Singh SC, Kent GM, Collier JS, Harding AJ, Orcutt JA (1998) Melt to mush variations in
555 crustal magma properties along the ridge crest at the southern East Pacific Rise.
556 Nature 394: 874-878.
557 Sinton JM, Detrick RS (1992) Mid-Ocean Ridge Magma Chambers. Journal of Geophysical
558 Research 97: 197-216
559 Smewing JD (1981) Mixing characteristics and compositional differences in mantle-derived
560 melts beneath spreading axes: evidence from cyclically layered rocks in the ophiolite
561 of north Oman. Journal of Geophysical Research 86: 2645-2659
562 Smith MC, Perfit MR, Jonasson IR (1994) Petrology and geochemistry of basalts from the
563 southern Juan de Fuca ridge: Controls on the spatial and temporal evolution of mid-
564 ocean ridge basalt. Journal of Geophysical Research 99: 4787-4812
565 Stakes DS, Perfit MR, Tivey MA, Caress DW, Ramirez TM, Maher N (2006) The Cleft
566 revealed: Geologic, magnetic, and morphologic evidence for construction of upper
567 oceanic crust along the southern Juan de Fuca Ridge. Geochemistry Geophysics
568 Geosystems 7, Q04003, doi: 10.1029/2005GC001038

569 Tivey MA (1996) Vertical magnetic structure of ocean crust determined from near-bottom
570 magnetic field measurements. Journal of Geophysical Research 101: 20275-20296
571 Tivey MA, Johnson HP, Fleutelot C, Hussenoeder SA, Lawrence R, Waters C, Wooding, B
572 (1998) Direct measurement of magnetic reversal polarity boundaries in a cross-section
573 of oceanic crust. Geophysical Research Letters 25: 3631-3634
574 Volpe AM, Goldstein SJ (1993) ^{226}Ra-^{230}Th disequilibrium in axial and off-axis mid-ocean
575 ridge basalts. Geochimica et Cosmochimica Acta 57: 1233-1241
576 Wanless VD, Perfit MR, Ridley WI, Klein E (2010) Dacite petrogenesis on Mid-Ocean
577 Ridges: Evidence for oceanic crustal melting and assimilation. Journal of Petrology
578 51: 2377-2410
579 West M, Menke W, Tolstoy M (2003) Focused magma supply at the intersection of the Cobb
580 hotspot and the Juan de Fuca ridge. Geophysical Research Letters 30: 1724
581 Wilson DS (1993) Confidence intervals for motion and deformation of the Juan de Fuca plate.
582 Journal of Geophysical Research 98: 16053-16071
583 Wilson DS, Hey RN, Nishimura C (1984) Propagation as a mechanism of reorientation of
584 Juan de Fuca Ridge. Journal of Geophysical Research 89: 9215-9225
585 Wilson DS et al (2006) Drilling to gabbro in intact ocean crust. Science 312: 1016-1020.
586

587 **Figure captions:**

588

589 Figure 1. Theoretical magma chamber considered in the mathematical modeling (a) and its
590 adaptation to fit with the different mechanisms proposed for the accretion of the lower
591 oceanic crust and for the related geometry of the magma chamber beneath fast to intermediate
592 spreading ridges (b and c). In the ‘‘Gabbro glacier’’ model (b), crystallization takes place in a
593 thin sill at the base of the sheeted dike complex from which cumulates subside down

(Henstock 2002; Henstock et al. 1993; Phipps Morgan and Chen 1993; Quick and Denlinger 1993). GG1 and GG2 refer to the two scenarios envisioned when discussing in the text the volume of melt expellable from the reservoir (with or without the contribution of the interstitial melt of the crystal mush, respectively). In the ‘‘Sheeted sill’’ model (c), the lower oceanic crust is formed through *in situ* crystallization of multiple sills (Boudier et al. 1996; Garrido et al. 2001; Kelemen et al. 1997; Korenaga and Kelemen 1998). The volume of expellable melt is then approached by considering the contribution of two melt lenses. The different parameters are defined in Table 1: *Q* refers to melt volumes, *C* to element concentrations, and the subscripts i, c and e to injected, crystallized and expelled, respectively. The wide arrows show the main melt fluxes through the magmatic system.

Figure 2. Chemical evolution of the lavas collected along the Cleft segment and the Northern Scarp of the Western Blanco Depression (WBD). a) Shaded relief bathymetry of the Cleft segment and WBD with the location of the submersible dives along the Northern Scarp (Cordier et al. 2007; Juteau et al. 1995) and of the Cleft segment samples (Smith et al. 1994; Stakes et al. 2005). Inset: location map of the WBD in the NE Pacific. JdF R.: Juan de Fuca ridge; G. R.: Gorda ridge; BTF: Blanco Transform Fault. b) Evolution of the MgO contents in lavas with latitude. c) TiO_2 versus MgO diagram. Samples used in the model resolution are labeled and their composition is listed in Table 2. Chemical data are from the literature (Smith et al. 1994; Stakes et al. 2005; Cordier et al., 2007).

Figure 3. Chemical evolution with depth in the extrusive unit of the Northern Scarp for two groups of dives, located ca. 25 and 40 km eastward from the Juan de Fuca axis, respectively. a) Lithologies observed along the Northern Scarp superimposed on the magnetic cross section (Tivey 1996; Tivey et al. 1998). Normal polarity crust is shaded in light gray (M: Matuyama)

and inverse polarity crust in dark gray (B: Brunhes, J: Jaramillo, 2: Anomaly 2). The filled stars show the position of the dives illustrated in b). b) Variations of La with depth. They are consistent with those of Mg# shown in Cordier et al. (2007) (their Fig, 10). The changes from mafic (low La contents) to intermediate or evolved terms (high La contents) are thought to result from fractional crystallization, followed by returns to mafic compositions during replenishment events.

Figure 4. Resolution procedure of the model of Rannou et al. (2006). Parameters are defined in Table 1. In the step 1, Eq. 1 is modified after Eq. 12 of Rannou et al. (2006). ω is fixed arbitrarily to 2π. f and z^E are new parameters with respect to the model of Rannou et al. (2006) and are used to model the mixing between the interstitial residual melts of the crystal mush zones and the melt residing in the lens.

Figure 5. Effect of the variation of the parameters C^E_{max}, f and Q_{max}-Q_{min} on the REE concentration in lavas (a and b) and on the resident melt volume (c and d). La is shown as an example of the REE concentrations in lavas. The curves are drawn using Eq. 1 and Eq. 6 (Fig. 4). The parameters C^{La}_{min} (3.1 µg/g), r_e (0.4) and [q_i] (0.004 km^3/yr.10km) are similar in the different illustrated cases. The values of f, C^E_{max} and Q_{max}-Q_{min} used in each case are stated on the figure. f is the fraction of interstitial melt migrating from the solidification zone into the melt lens. f=1 when the melt lens collects the entire volume of the melts that have evolved in the solidification zones (perfect fractional crystallization). f=0.5 when half of the melts that have evolved in the solidification zones are injected within the melt lens. The results for each calculation are listed in Table 3. The model does not give suitable solution for f = 0.5 and C^{La}_{max} = 20.6 µg/g (b).

644 Figure 6. Chemical compositions used for the model resolution and results of the first step of
645 the modeling. (a) The range of REE compositions of the Northern Scarp lavas, the C^{E}_{min} and
646 C^{E}_{max} used in the modeling (listed in Table 2) and the Mg#70 melt composition deduced by
647 Cordier et al. (2007) from petrological and geochemical data are shown. (b) Composition of
648 the replenishment melt (C^{E}_{i}, Table 3) together with the lava range (see text). C^{E}_{i} are calculated
649 graphically for each REE by introducing into Eq. 1 of Fig. 4 the following parameters: r_e =
650 0.4; C^{E}_{max} = REE contents in Fe-basalt and andesite, respectively (Table 2); f=0.5 and f=1.
651 The theoretical C^{E}_{i} patterns have lower REE contents than the lavas and are slightly more
652 depleted in LREE. The spectrum of the Mg#=70 primary melt is very close to and bracketed
653 by our theoretical refilling melts. The model does not give suitable C^{E}_{i} pattern for f = 0.5 and
654 C^{E}_{max} (andesite).
655

Table 1. Definition of the model parameters.

Parameters	Values[a]	Definition
C^E_{max} (µg/g)	Table 2	Concentration of the rare earth element E in the most evolved lava
C^E_{min} (µg/g)	Table 2	Concentration of E in the most mafic lava
C_i^E (µg/g)		Concentration of E in the refilling melt
D^E	Table 2	Bulk distribution coefficient of E
f [b]	0.5 and 1	Fraction of melt evolving in the solidification zones and reintroduced in the melt lens
z^E [b]	Table 2	Coefficient accounting for melt differentiation due to fractional crystallization and possible chemical exchanges between melt and crystals in crystal mush
$[q_i]$ (km^3/yr.10km)[c]	0.004	Average rate of melt input in the reservoir
α (yr^{-1})		Average crystallization rate: fraction of melt crystallized per time unit
$\omega/2\pi$ (Hz)		Frequency of the replenishment, with ω the pulsation of the replenishment
β^E		Internal parameter iteratively estimated for each E, the average of which gives β_{av}
β_{av}		Ratio between pulsation (ω) and crystallization rate (α), average of the β^E values
r_e	0.4	Mean ratio between average extrusion and crystallization rates
Q (km^3/yr.10km)[c]		Volume of melt residing (i.e. expellable) in the reservoir
Q_{max}-Q_{min} (km^3/10km)[c]	0.45 to 0.90	Amplitude of the variations of the melt volume in the reservoir
T (yr)		Period of the replenishment
τ (yr)		Average magma residence time

[a] Values introduced into the resolution procedure are stated here when constant for the different REEs. Otherwise, they are listed in Table 2.

[b] Parameters adapted from the equations of *in situ* crystallization of Langmuir (1989).

[c] Units are expressed for a 10 km-long magma chamber, as typically observed beneath the Cleft segment. See text.

Table 2. Chemical input parameters.

Sample	2960-7	BN02-12	999-1B	RC-10				
Parameter[a]	C^E_{min}	C^E_{max}	C^E_{max}		$z_1^{E\,b}$	$z_2^{E\,b}$	$z_1^{E\,b}$	$z_2^{E\,b}$
Type[c]	Bas.	Fe-bas.	And.	Dac.	→Fe-bas.	→And.	→Fe-bas.	→And.
f					1	1	0.5	0.5
Loc.[d]	NS	NS	Galap.	Cleft				
Analysis[e]	WR	WR	GL	GL				
Ref.[f]	1	1	2	3				
SiO_2 (wt. %)	49.50	48.85	56.70	63.15				
TiO_2	1.36	3.61	1.91	1.29				
Al_2O_3	15.15	11.62	11.42	12.47				
$Fe_2O_3^{tot\,g}$	10.80	19.10	17.98	11.84				
MnO	0.19	0.26	0.29	0.18				
MgO	8.05	4.27	1.80	1.13				
CaO	12.00	7.78	6.90	4.52				
Na_2O	2.30	3.10	3.48	4.43				
K_2O	0.15	0.34	0.39	0.98				
P_2O_5	0.14	0.52	0.65	-				
LOI	-0.15	1.08	-	-				
Total	99.49	100.53	101.52	99.99				
Mg#[h]	64.85	35.62	22.07	23.95				
La (µg/g)	3.1	13.3	20.6		0.06	0.09	0.11	0.16
Ce	9.6	42	61		0.06	0.10	0.11	0.19
Nd	8.3	40	58		0.11	0.18	0.20	0.30
Sm	3.05	-	18.2		0.17	0.27	0.30	0.42
Eu	1.09	3.30	4.82		0.21	0.29	0.35	0.45
Gd	4.25	-	23.5		0.22	0.32	0.35	0.49
Dy	5.25	16.2	27.0		0.22	0.33	0.37	0.50
Er	3.10	10.7	18.8		0.23	0.33	0.37	0.49
Yb	3.10	9.65	17.6		0.22	0.30	0.36	0.46

[a] Parameters are defined in Table 1.

[b] The z^E values are calculated from the bulk partition coefficients D^E (Table 1), considering two *f* values (1 and 0.5) and two cumulate modal compositions: 0.10 ol + 0.35 cpx + 0.55 plag for z_1^E (Rannou et al. 2006) and 0.043 ol + 0.447 cpx + 0.452 plag + 0.055 tmt + 0.003 ap for z_2^E (Perfit et al. 1983). Note that when $f = 1$, z^E and D^E are equivalent.

[c] Bas. = basalt; Fe-bas. = ferrobasalt; And. = andesite; Dac. = dacite.

[d] Location: NS = Northern Scarp; Galap. = Eastern Galapagos rift; Cleft = south Cleft segment.

[e] WR = whole-rock analysis (ICP-AES); GL = glass analysis (EPMA).

[f] References: 1. Cordier et al. (2007); 2. Fornari et al. (1983) and Perfit et al. (1983); 3. Stakes et al. (2006).

[g] All Iron as $Fe_2O_3^{tot}$.

[h] Mg# is calculated using a Fe_2O_3/FeO ratio of 0.2, 0.3 and 0.4 for basalt/ferrobasalt, andesite, and dacite, respectively.

Table 3. Results of the modeling for the Cleft segment magma system in function of different values of C^{E}_{max}, f and Q_{max}-Q_{min} but similar values of C^{E}_{min} (Table 2), r_e (0.4) and [q_i] (0.004 km3/yr.10km).

C^{E}_{max} [1]	Fe-bas	Fe-bas	Andesite	Mg#=70
f	1	0.5	1	
Step 1: Composition of the modeled replenishment melt				
La (µg/g)	1.42	1.54	1.52	1.35
Ce	4.41	4.82	4.85	4.37
Nd	4.19	4.75	4.67	4.13
Sm			1.90	
Eu	0.62	0.72	0.70	0.69
Gd			2.80	
Dy	3.03	3.56	3.50	3.08
Er	1.82	2.13	2.05	1.90
Yb	1.78	2.09	2.02	1.83
β^{REE}	0.930-1.285	0.715-1.048	0.141-0.730	
β_{av}	1.137	0.899	0.467	
$\sigma(\beta_{av})$ [2]	0.119	0.124	0.200	
Step 2: Crystallization rate (α), period (T), residence time (τ)				
GG[3], Q_{max}-Q_{min} = 0.45 km^3/10km				
α (yr^{-1})	0.0099	0.0107	0.0121	
T (yr)	561	654	1118	
τ (yr)	72	67	59	
GG[3], Q_{max}-Q_{min} = 0.63 km^3/10km				
α	0.0070	0.0076	0.0086	
T	785	916	1565	
τ	101	94	83	
SS[3], Q_{max}-Q_{min} = 0.9 km^3/10km				
α	0.0049	0.0053	0.0060	
T	1122	1308	2235	
τ	145	134	119	

[1] C_{max}: composition of the most evolved lava considered in our calculations.
[2] $\sigma(\beta_{av})$: standard deviation of the β^E values deduced from the different REE.
[3] GG: gabbro glacier model for the magma chamber, by ignoring or considering the partial draining of the crystal much lying beneath the melt lens; SS: sheeted sill model. See text for the estimation of the different volumes.

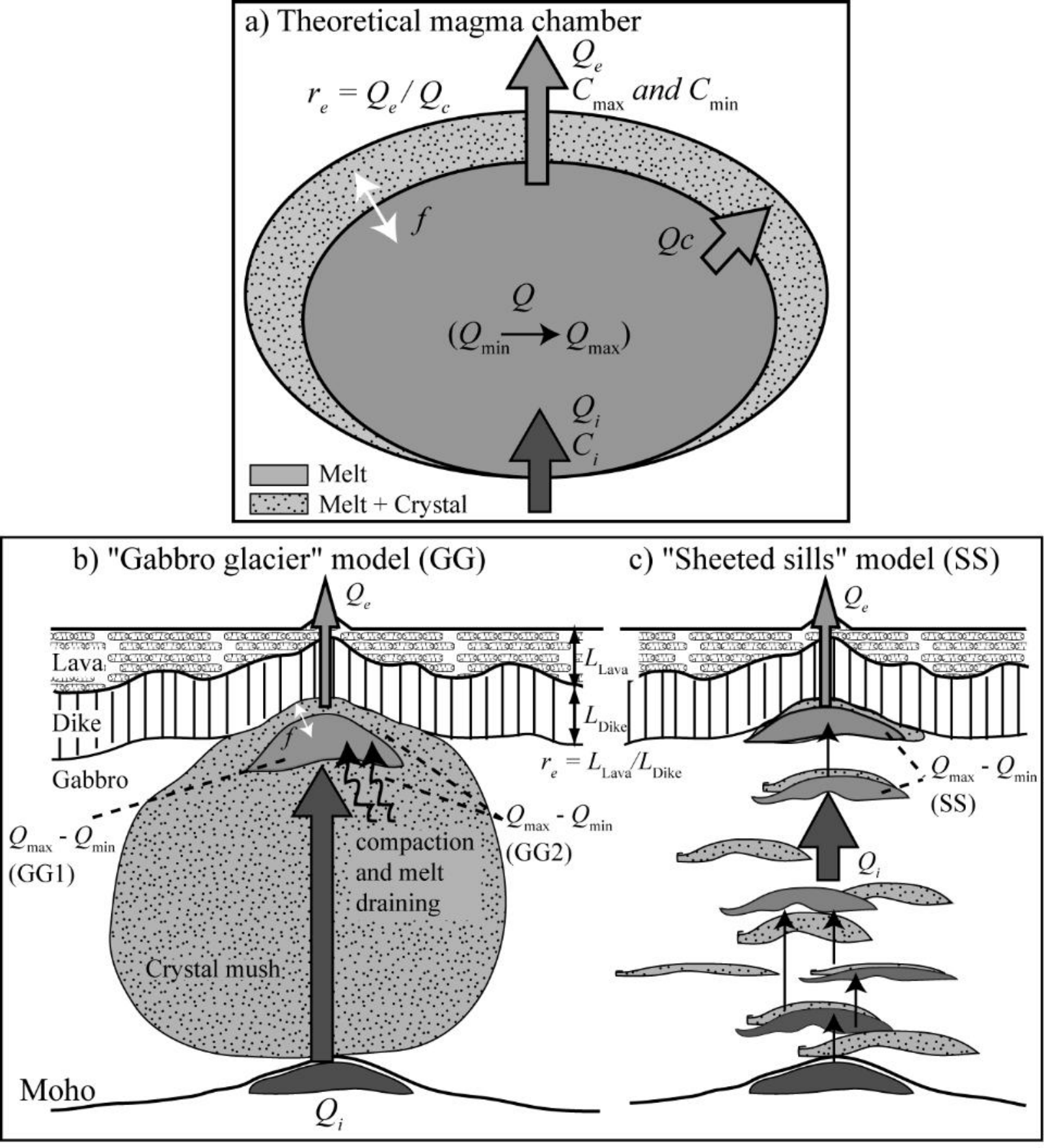

Cordier et al.
Figure 1

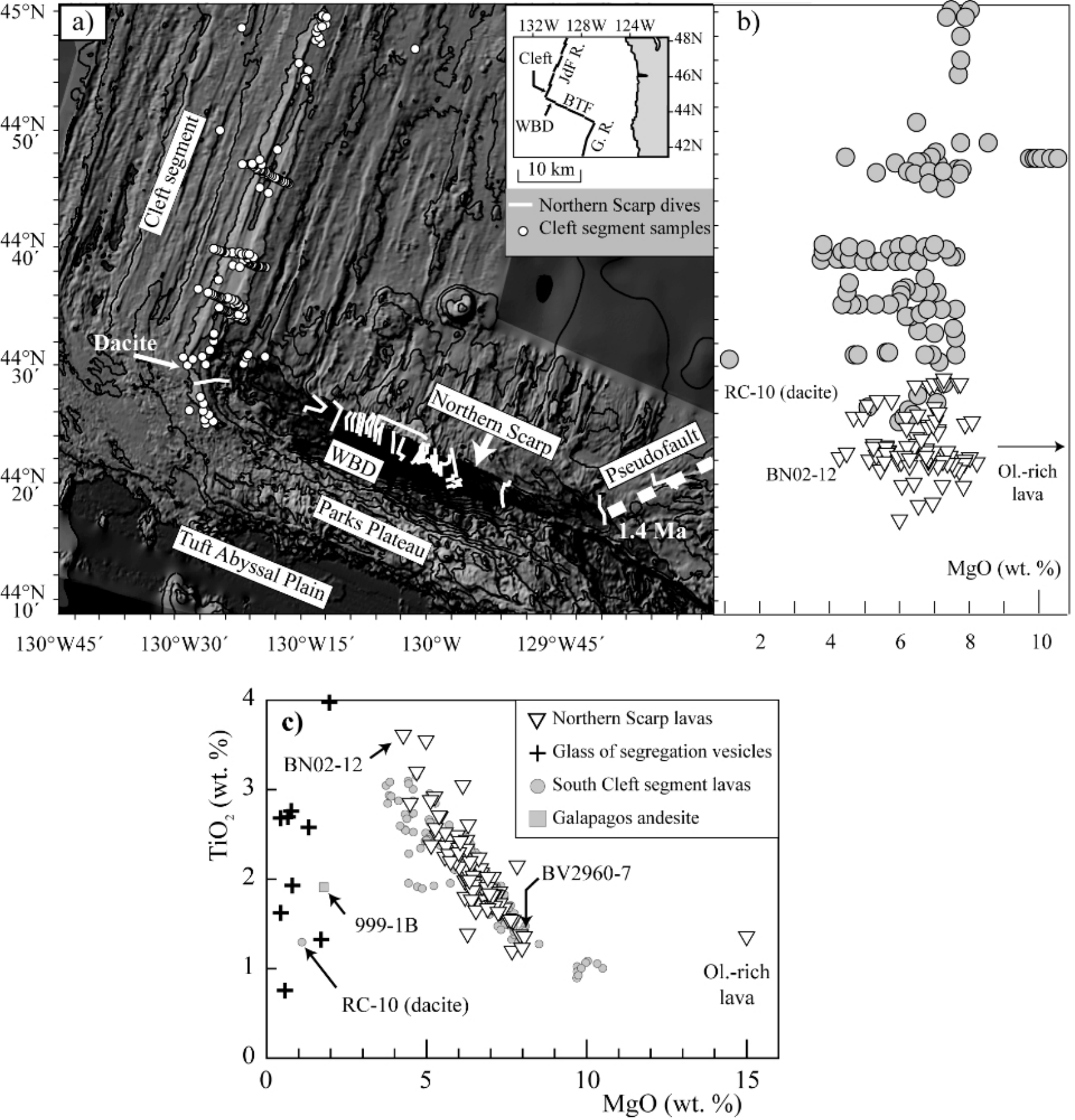

Figure 2
Cordier et al.

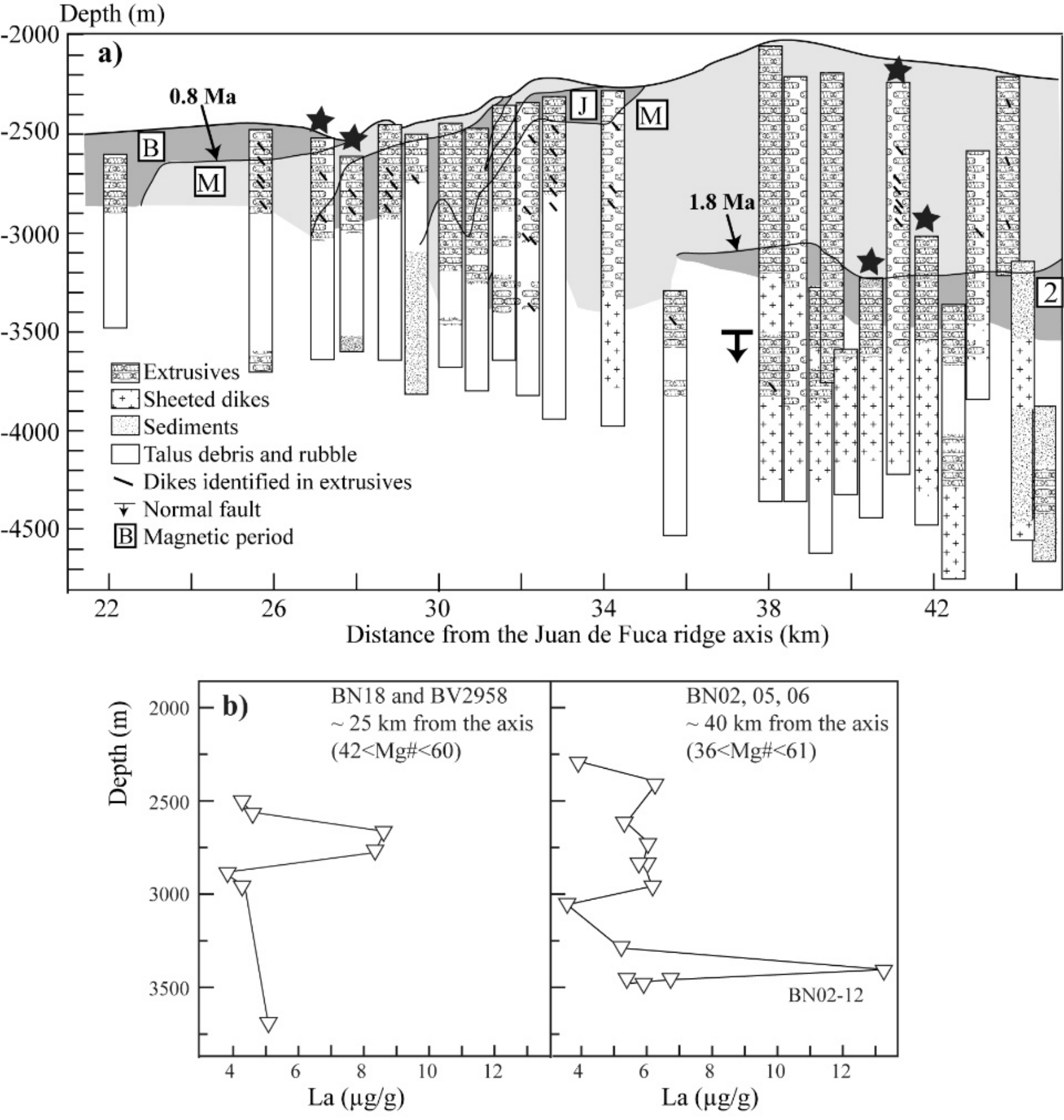

Figure 3
Cordier et al.

(a) Step 1: Geochemical approach

Required parameters:

C^{E}_{min}

C^{E}_{max}

D^{E}

r_e

f

Eq. 1:
$$C^{E}(t) = C_i^{E} \frac{\frac{1}{z^{E} + r_e} + \left[\frac{\cos\left(\omega t - \arcsin \frac{\beta^{E}}{\sqrt{\beta^{E2} + (z^{E} + r_e)^2}}\right)}{\sqrt{\beta^{E2} + (z^{E} + r_e)^2}} \right]}{\frac{1}{1 + r_e} + \left[\frac{\cos\left(\omega t - \arcsin \frac{\beta^{E}}{\sqrt{\beta^{E2} + (1 + r_e)^2}}\right)}{\sqrt{\beta^{E2} + (1 + r_e)^2}} \right]}$$

With Eq. 2:
$$z^{E} = \frac{D^{E}}{D^{E}(1 - f) + f}$$

Results: β^{E}, β_{av} and C_i^{E}

(b) Step 2: Temporal approach

Required parameters:

β_{av}

$[q_i]$

r_e

$Q_{max} - Q_{min}$

Eq. 3:
$$\alpha = \frac{2[q_i]}{(Q_{max} - Q_{min})\sqrt{\beta_{av}^2 + (1 + r_e)^2}}$$

Eq. 4:
$$T = \frac{2\pi}{\alpha \beta_{av}}$$

Eq. 5:
$$\tau = \frac{1}{\alpha(1 + r_e)}$$

Eq. 6:
$$Q(t) = \frac{[q_i]}{\alpha(1 + r_e)} + \frac{[q_i] \cos\left[\frac{2\pi}{T} t - \arcsin\left(\frac{\beta_{av}}{\sqrt{\beta_{av}^2 + (1 + r_e)^2}}\right)\right]}{\sqrt{\alpha^2(1 + r_e)^2 + \left[\frac{2\pi}{T}\right]^2}}$$

Results: α, T, τ, and Q

Figure 4
Cordier et al.

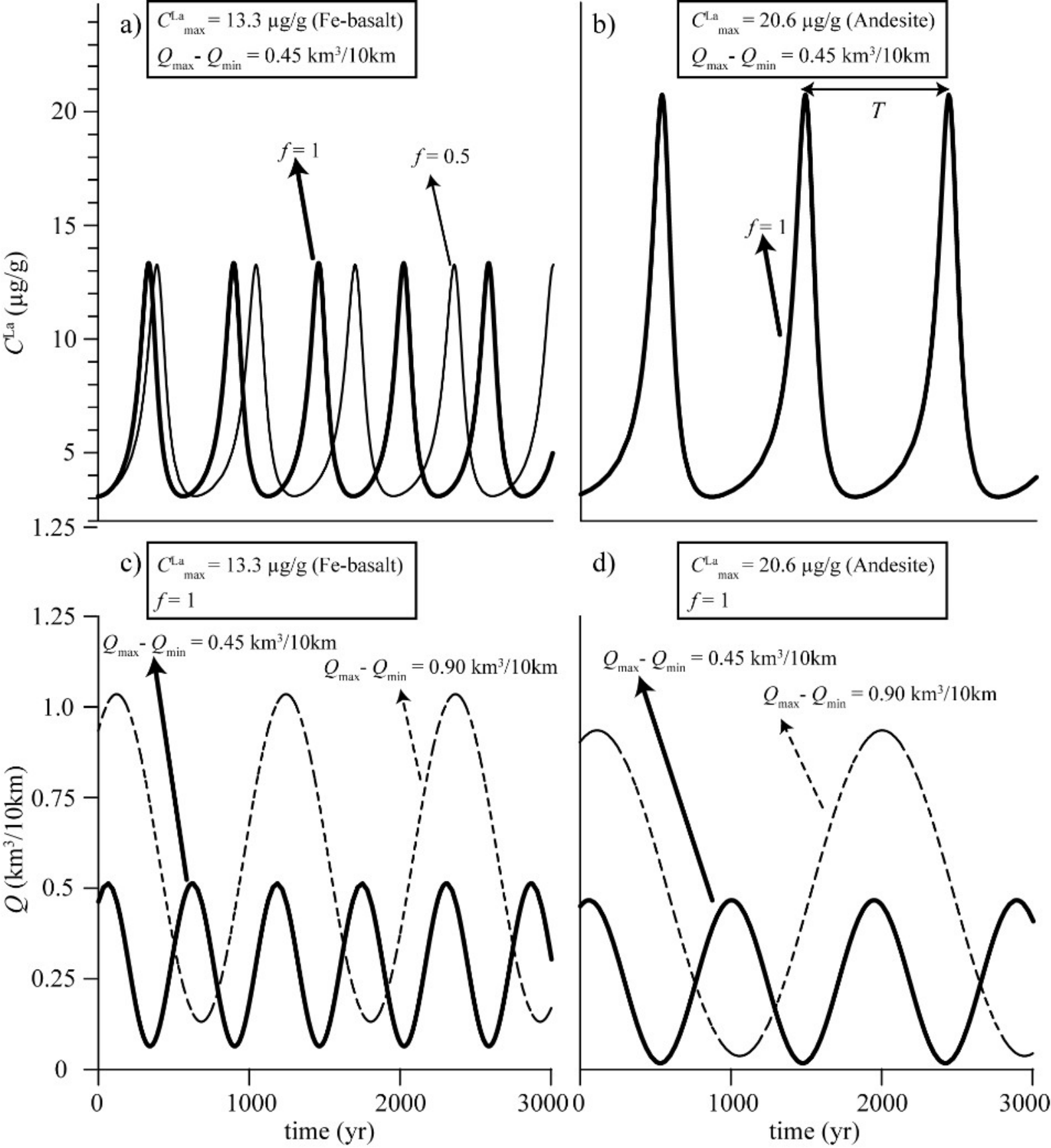

Cordier et al.
Figure 5

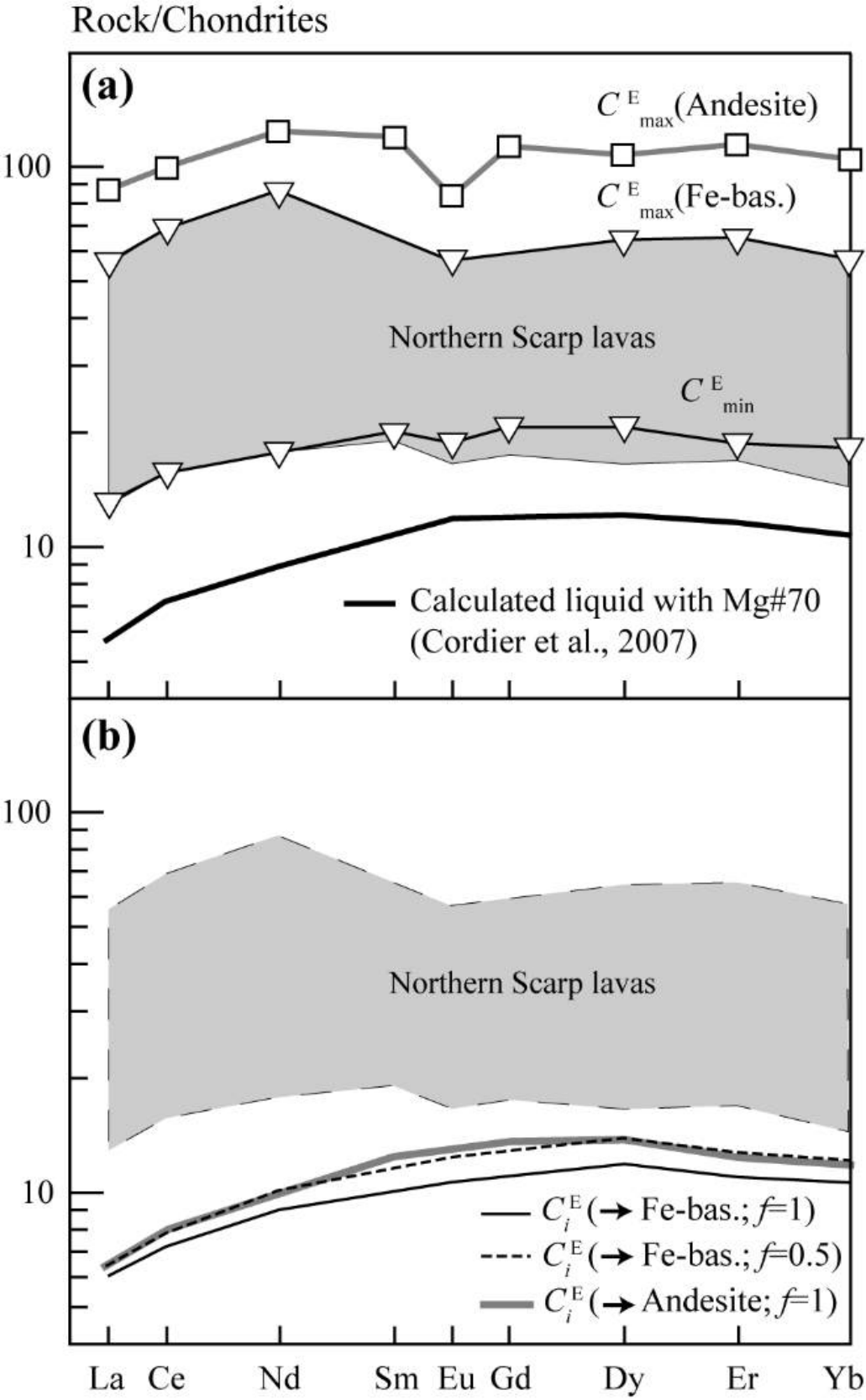

Cordier et al.
Figure 6